*Original Article*

*Journal of Sandwich Structures and Materials*

# Impact resistance of Nomex honeycomb sandwich structures with thin fibre reinforced polymer facesheets

DOI: 10.1177/1099636216664076

**Longquan Liu[1], Han Feng[1], Huaqing Tang[1] and Zhongwei Guan[2]**

**Abstract**

In order to investigate the impact resistance of the Nomex honeycomb sandwich structures skinned with thin fibre reinforced woven fabric composites, both drop-weight experimental work and meso-mechanical finite element modelling were conducted and the corresponding output was compared. Drop-weight impact tests with different impact parameters, including impact energy, impactor mass and facesheets, were carried out on Nomex honeycomb-cored sandwich structures. It was found that the impact resistance and the penetration depth of the Nomex honeycomb sandwich structures were significantly influenced by the impact energy. However, for impact energies that cause full perforation, the impact resistance is characterized with almost the same initial stiffness and peak force. The impactor mass has little influence on the impact response and the perforation force is primarily dependent on the thickness of the facesheet, which generally varies linearly with it. In the numerical simulation, a comprehensive finite element model was developed which considers all the constituent materials of the Nomex honeycomb, i.e. aramid paper, phenolic resin, and the micro-structure of the honeycomb wall. The model was validated against the corresponding experimental results and then further applied to study the effects of various impact angles on the response of the honeycomb. It was found that both the impact resistance and the

[1]School of Aeronautics and Astronautics, Shanghai Jiao Tong University, Shanghai, China
[2]School of Engineering, University of Liverpool, Liverpool, UK

**Corresponding author:**
Longquan Liu, School of Aeronautics and Astronautics, Shanghai Jiao Tong University, 800 Dongchuan Rd., Minhang District, Shanghai 20040, China.
Email: liulongquan76@sjtu.edu.cn

perforation depth are significantly influenced by the impact angle. The former increases with the obliquity, while the latter decreases with it. The orientation of the Nomex core has little effect on the impact response, while the angle between the impact direction and the fibre direction of the facesheets has a great influence on the impact response.

**Keywords**
Nomex honeycomb sandwich, fibre reinforced polymer facesheet, impact resistance, oblique angle, finite element

## Introduction

The sandwich structures with Nomex honeycomb core and fibre reinforced composite facesheets are increasingly used in aviation industry, due to the combined advantages of the Nomex honeycomb core and fibre reinforced polymer (FRP) skins. However, because of the thin nature of the facesheets, the honeycomb sandwich structures are very sensitive to the impact loading caused by runway debris, hailstones, dropped tools, etc. [1–5]. The facesheets can be easily perforated by a projectile when the impact energy is above a certain value. After perforation, the mechanical performance of the sandwich structures is likely to be deteriorated due to water and/or moisture being passed inside the structures. The water and/or moisture collected in the core during service would cause further damage and weight increase. In the worse scenarios, the control systems and instruments could be damaged directly by a high-energy impact accident. As a result, the aviation safety would be jeopardized.

Extensive research work was conducted on the mechanical response of the Nomex honeycomb sandwich structures under impact loading [6–11]. However, limited research work was undertaken on the perforation failure of honeycomb sandwich structures and most of these studies were focused on normal impact, i.e. the impact direction is perpendicular to the surface of a target. This is not always the case in real scenarios as the angle of impact is variable. The energy absorbing behaviour under an oblique impact loading can be significantly different and the stress state and failure mode of the honeycomb sandwich structures are even more complicated. The theoretical approach is not applicable to predict such complex deformations and failure mechanisms. It is also difficult and expensive to undertake oblique impact tests. Due to its manufacturing process, the mechanical properties of the Nomex honeycomb core are different in the L-direction (ribbon direction), W-direction (direction perpendicular to the ribbon), and the T-direction (out-of-plane direction or through-the-thickness direction). Therefore, the finite element method is an effective means to be used to evaluate the oblique impact resistance of the Nomex honeycomb sandwich structures with different material and geometrical parameters of the Nomex honeycomb core.

The impact response, together with the interaction between the projectile and sandwich structures, is significantly different from those of monolithic laminate, since the honeycomb core is much softer than the facesheets in the out-of-plane direction. Therefore, the mechanical behaviour of the core material must be well characterized in order to analyse the indentation and perforation of sandwich structures and to simulate the contact conditions and further the damage. In the finite element modelling of the impact response of the honeycomb sandwich structures, the core is usually modelled by the equivalent spring elements [12,13] or by the equivalent three-dimensional continuum elements [4,6,8,9,14–18]. Since such an approach does not take the real cellular structure into consideration, the sandwich core is instead analysed in terms of its effective properties. Here, the mechanical characteristics of the Nomex honeycomb under both the flatwise stress and the off-axis stress are required. Therefore, extensive tests need to be conducted in different loading directions, due to the in-plane anisotropy of the Nomex honeycomb core [19–25]. Furthermore, this approach can only be used to simulate the global responses phenomenologically, but cannot be used to predict the real failure mechanisms, since it did not consider the details of the structural characteristics of the Nomex paper.

The basic material of the Nomex honeycomb core is phenolic resin-impregnated aramid paper and the cell wall is essentially a laminated structure due to its manufacturing processes [26]. The mechanical properties of the aramid paper and the phenolic resin are usually different. Also, the mechanical properties of the Nomex honeycomb core depend on the constituent materials and their proportion, as well as the geometrical parameters of the core. The virtual testing method, which is based on the finite element modelling using parameters of the constituent materials and validated by sufficient test results, can be used to simulate complex loading conditions with certain requirements. This approach is very efficient and cost effective [27]. Therefore, based on the idea of virtual testing, a meso-scale finite element model was proposed and developed to represent the layered structure of the core. It was used to investigate the mechanical behaviour of the Nomex honeycomb sandwich structure subjected to oblique impact. Therefore, in this paper, the impact response of the Nomex honeycomb sandwich structures with thin FRP facesheets was investigated both experimentally and numerically by considering the influences of impact energy, velocity, mass, thickness of the two facesheets, and oblique angles.

## Normal impact tests of the Nomex honeycomb sandwich structures

### *Specimen description*

A typical Nomex honeycomb sandwich structure is shown in Figure 1. It consists of one Nomex honeycomb core and two fibre reinforced woven fabric composite facesheets. The 'L', '*W*', and 'T' directions of the honeycomb are coincident with

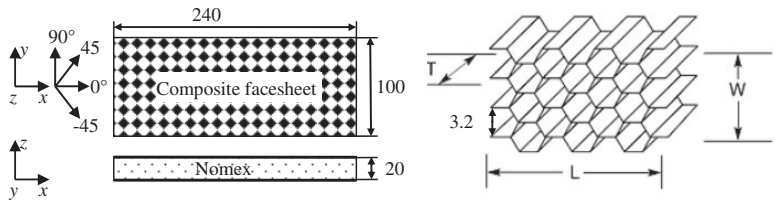


**Figure 1.** Geometry of Nomex honeycomb sandwich (all dimension in mm): Nomex honeycomb sandwich (left) and Nomex honeycomb core (right).

the 'x', 'y', and 'z' directions of the coordinate system of the specimen shown in Figure1(a), respectively. The '1' (fill or weft), '2' (Warp), and '3' (out-of-plane) directions of lamina with 0° ply angle are also coincident with the 'x', 'y', and 'z' directions, respectively.

The core is made of regular hexagonal Nomex honeycombs, with the cell size and density being 3.2 mm and 48 kg/m$^3$, respectively. The honeycombs were made from Nomex aramid paper with a nominal thickness of 0.05 mm and an areal density of 40 g/m$^2$. The three material directions of the honeycomb core are illustrated in Figure 1(b). Both the single and double cell walls are layered structure. The single cell wall consists of two resin layers and an aramid paper layer, with each resin layer being 0.008 mm thick and paper layer being 0.054 mm thick. The aramid paper layer is understandably placed between the two resin layers. The double cell wall consists of two resin layers and two aramid paper layers. The two layers of aramid paper are glued together. The thicknesses of the resin layer and paper layer in the double cell wall are the same as those in the single cell wall. Therefore, the total thickness of the resin-dipped honeycomb single cell wall is 0.07 mm, and that of the double cell wall is 0.124 mm. The elastic modulus of the phenolic resin is 5.8 GPa, strength is 60 MPa, Poisson's ratio is 0.389, elongation at break is 1%, and density is 1380 kg/m$^3$ [28]. The material properties of the aramid paper and phenolic resin are shown in Table 1. In the table, $E_{MD}$ and $E_{XD}$ represent the elastic modulus in the machine direction (MD) and the cross machine direction (XD), $S_{MD}$ and $S_{XD}$ represent the tensile strengths in these two directions, $\delta_{MD}$ and $\delta_{XD}$ refer to the elongation at break again also in these two directions, $\mu$ is the Poisson's ratio and $\rho$ is the density.

Three groups of Nomex honeycomb-cored sandwich specimen and one group of laminates were tested and the geometric configurations of the specimens are shown in Table 2. Here, the '(±45)' for the facesheet indicates a plain woven fabric lamina with a ply angle of 45°, the subscripts '3', '2', and '9' indicate the ply number and the 'core' indicates the Nomex honeycomb core. The core thickness of all sandwich specimens (Specimens 1, 2, and 3) is 20 mm and the thickness of the lamina used in the facesheets is 0.216 mm. The laminate specimens (Specimen 4) have the same surface area as that of the sandwich specimens. The mechanical properties of the woven fabric lamina are shown in Table 3, where $E_i$ ($i = 1, 2, 3$) are the elastic modulus of the woven fabric lamina in fill, warp, and thickness directions.

**Table 1.** Material properties of the aramid paper [28].

| | $E_{MD}$ (GPa) | $E_{XD}$ (GPa) | $S_{MD}$ (MPa) | $S_{XD}$ (MPa) | $\delta_{MD}$ (%) | $\delta_{XD}$ (%) | $\mu$ (−) | $\rho$ (kg/m$^3$) |
|---|---|---|---|---|---|---|---|---|
| Value | 3.1 | 1.6 | 88 | 35 | 9.6 | 6.5 | 0.3 | 740 |

**Table 2.** Geometry configurations of the specimens.

| Configuration | Stacking sequence |
|---|---|
| Specimen 1 | $[(\pm45)_3$/Core/ $(\pm45)_2]$ |
| Specimen 2 | $[(\pm45)_9$/Core/ $(\pm45)_9]$ |
| Specimen 3 | $[(\pm45)_2$/Core/ $(\pm45)_3]$ |
| Specimen 4 | $[(\pm45)_{18}]$ |

**Table 3.** Mechanical properties of Carbon/Epoxy plain woven fabric lamina.

| | | | |
|---|---|---|---|
| $E_1 = E_2 = 48$ GPa | $E_3 = 10.3$ GPa | $S_1^T = S_2^T = 585$ MPa | $S_1^C = S_2^C = 585$ MPa |
| $\mu_{12} = 0.042$ | $\mu_{31} = \mu_{23} = 0.26$ | $S_3^T = 48.5$ MPa | $S_3^C = 250$ MPa |
| $G_{12} = 5.2$ GPa | $G_{31} = G_{23} = 4.5$ GPa | $S_{12} = 140$ MPa | $S_{31} = S_{23} = 120$ MPa |

$G_{ij}$ $(i = 1, 2, 3)$ are the shear modulus, $\mu_{ij}$ $(i = 1, 2, 3)$ are the Poisson's ratios, and $S_{ij}(i = 1, 2, 3)$ are the material strengths. The superscripts T and C denote tension and compression, respectively. The density of the woven fabric lamina is 1540 kg/m$^3$.

## *Impact tests*

The impact tests were conducted in accordance with the material test standard, ASTM D3763-02 [29] on an Instron Ceast 9350 drop-weight testing machine. Five repeated tests were conducted for each case with different impact parameters. Figure 2 shows the test setup. The test specimen was fixed by two clamping rings on both faces of the sandwich. The clamping rings consist of two parallel rigid plates with a 76 mm diameter hole in the centre. The edge of the hole was rounded to a radius of 0.8 mm. Initial pressure force of 50 N was applied on the upper clamping ring, which was fixed to prevent slippage of the specimen in the clamp during impact. The steel impactor consists of a 12.7 mm diameter steel rod with a hemispherical end of the same diameter. The impactor mass is 2.631 kg, with a hardness of 62 HRC. The impact location is at the centre of the upper ring. During impacting, the impactor's displacement, force and velocity were measured in real-time with the built-in sensors in the testing machine. The data were recorded at a sampling rate of 1000 data per second.

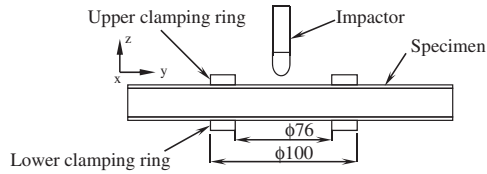


**Figure 2.** Diagram of impact test setup (all dimensions in mm).

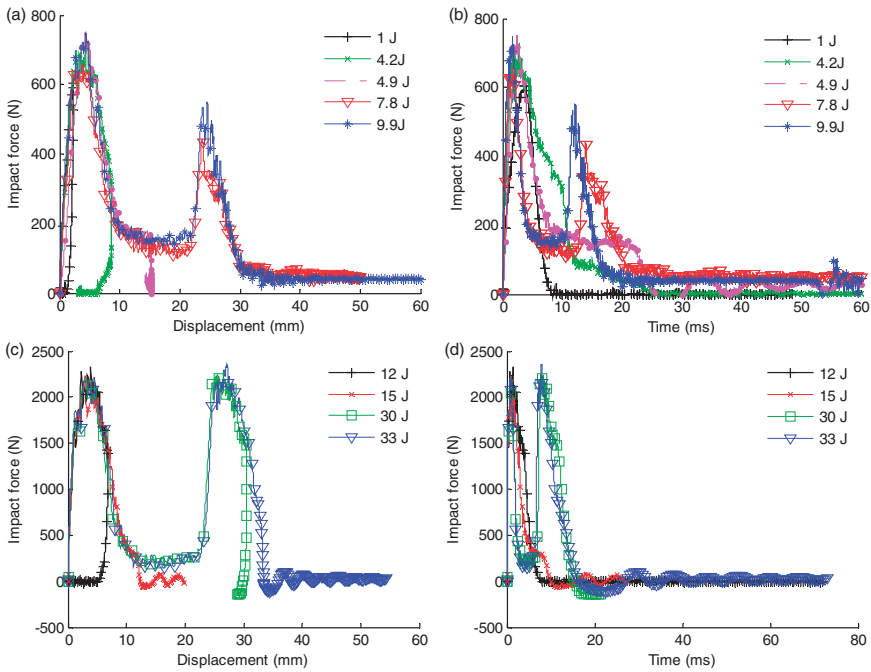


**Figure 3.** The influence of the impact energy: (a) force–displacement curves of Specimen 1, (b) force–time curves of Specimen 1, (c) force–displacement curves of Specimen 2, and (d) force–time curves of Specimen 2.

## Analysis of experimental results

### *Effect of impact energy*

The test results of Specimen 1 and Specimen 3 in relation to different impact energies are shown in Figure 3. Figure 3(a) and (b) exhibits the impact force–displacement and impact force–time curves of the Specimen 1, while Figure 3(c) and (d) shows such curves of the Specimen 3. From Figures3(a) and (b), it can be seen that the 3-layer top facesheet of the sandwich was damaged but not perforated when the impact energy is 4.2 J. However, with the energy increased

to 4.9 J only the upper facesheet was perforated. Consequently, when the impact energy was further increased to 7.8 J the sandwich structure was fully perforated. The results indicate that the 3-layer top facesheet was perforated when the impact energy is between 4.2 J and 4.9 J, while both the top and bottom facesheets were perforated when the impact energy is between 4.9 J and 7.8 J. It is interesting to note that the load–displacement curves with different impact energy are almost the same before the end of each impact process. The peak impact forces are similar, around 750 N, except for the case of the impact energy of 1 J, which is about 620 N, since it is not high enough to make the impact force reach the ultimate peak. The contact stiffnesses of the all loading cases are also similar. There are no significant fluctuations in the force–displacement curves before the impact forces reach their summit, which indicates that there is no obvious delamination that occurred in the facesheet in this stage.

For the case with the impact energy of 1 J, the contact force rises up linearly to its peak about 620 N, followed by a steep drop back to 0 N due to the impactor rebound. When the impact energy is increased to 7.8 and 9.9 J, the load–displacement curves indicate the similar saddle shape. The first peak value is about 750 N with a displacement of 5 mm and the second one is about 500 N with a displacement of 25 mm. There are plateau loads of about 150 N between the two peaks. There is no significant difference between the load–displacement curves related to these two energies, although the second peak value of the 9.9 J impact is higher than the other one. In the case of the impact energy of 4.2 J, the impact force–displacement curve follows the similar trend of the 9.9 J case until the projectile starts to bounce back, left with an indentation of about 8 mm. With the impact energy increased to 4.9 J, the trend of the force–displacement is again similar, but the permanent displacement is almost doubled.

However, the impact force–time curves show different responses with different impact energies (Figure 3(b)). The response time of the case with a higher impact energy (so a higher initial velocity) is understandably shorter than those cases with lower impact energies.

From Figure 3(c) and (d), it can be seen that the impact force–displacement and impact force–time curves of the Specimen 2 follow the same pattern with those of Specimen 1 generally. The difference is the two peak values of the impact force are almost the same at about 2360 N, since both the top and bottom facesheets are 9-layer laminates. The top facesheet was perforated when the impact energy is between 12 J and 15 J. Both the two facesheets were perforated when the energy is either 30 J or 33 J.

## *Effect of the impactor mass*

Figure 4 shows the test results of Specimen 1 with different impactor masses. From the figure, it can be seen that the impactor mass has little effect on the impact process, although both the deformation and contact time are somewhat larger and longer for the higher impactor mass.

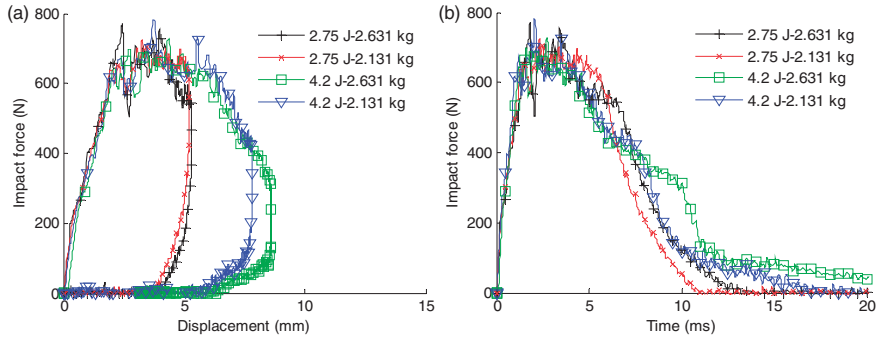


**Figure 4.** The influence of the impactor mass: impact force–displacement curves (left) and impact force–time curves (right).

## *Effect of the facesheet stacking sequence*

The top and bottom facesheets of Specimen 1 are 3- and 2-layer laminates respectively, and that of the Specimen 3 are 2- and 3-layered laminates, respectively. The geometries of these two specimens are actually the same and however, the penetration process of the impactor is inversed during the impact. The comparison of the impact test results of these two specimens is shown in Figure 5. From the figure, it can be seen that the perforation forces of the sandwich structures with 2- and 3-layered laminates on top are 750 N and 500 N respectively, which indicate that the facesheet stacking sequence has little effect on the ultimate impact force. Both the ultimate impact depth and the contacting time of the sandwich with 3-layer laminates on top is lower when the impact energy is 2.75 J; however, the contact stiffness is increased with the thickness of the top facesheet.

## *Effect of the thickness of the facesheet on perforation force*

From Figures 3 and 5, it can also be seen that, as the honeycomb sandwich is perforated, the perforation forces are about 500 N for the 2-layered laminated facing, 750 N for the 3-layered laminated facing, and 2360 N for the 9-layered laminated facing. This indicates that the perforation force is generally linear with the thickness of the facesheet.

## *Comparison between the honeycomb sandwich and the laminates*

The test results of Specimen 2 and Specimen 4 with the same impact energy of 33 J are shown in Figure 6. The figure indicates that the perforation force of the honeycomb sandwich is about 2360 N and that of the laminate is about 4850 N. The latter is more than two times of the former. The initial contact stiffness of the honeycomb sandwich structure is about 1767 N/mm and that of the laminate is about 2400 N/mm. The former is about two-thirds of the latter though the bending

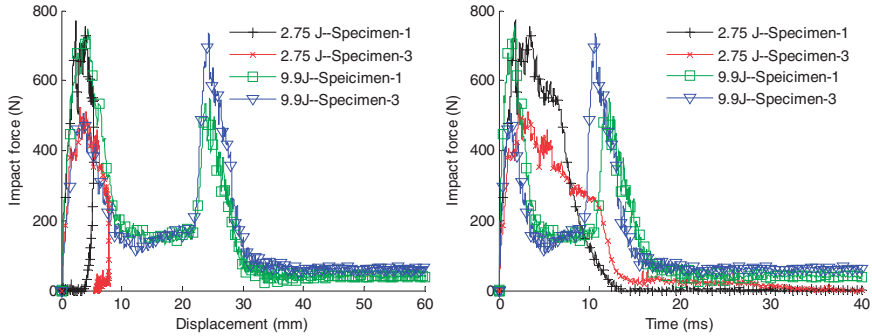


**Figure 5.** The influence of the impact sequence: impact force–displacement curves (left) and impact force–time curves (right).

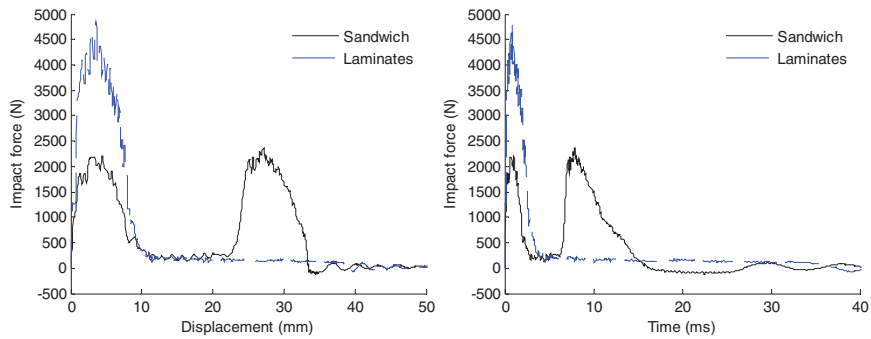


**Figure 6.** Comparison between Honeycomb sandwich and laminates: impact force–displacement curves (left) and impact force–time curves (right).

stiffness of the sandwich plate is much larger than that of the laminate. This indicates that the impacting stiffness of the sandwich structure is dominated by the local indentation of the impacted object rather than the global bending deformation.

From Figure 6, it can also be seen that there were some oscillations on the impact force of the honeycomb sandwich structure after it was perforated. This is because the impact force was not obtained through a transducer built in the impactor but indirectly through the mass and acceleration of the impactor. There are some small vibrations on the sandwich structure and the impactor after the top and bottom facesheets were perforated.

## Finite element simulations

### *Constitutive model of the aramid paper and phenolic resin*

The constitutive relationships of the aramid paper and phenolic resin are illustrated in Figure 7. The aramid paper was modelled as an elasto-perfectly plastic material,

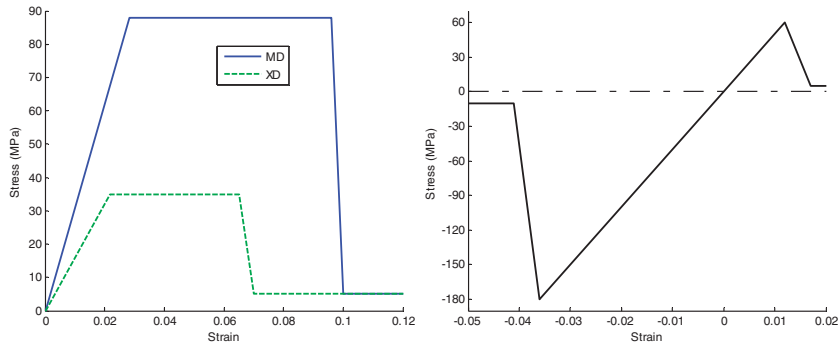


**Figure 7.** Constitutive models of the phenolic resin and aramid paper: aramid paper (left) and (b) phenolic resin (right).

where its compressive strength is assumed to be the same as its tensile counterpart. The aramid paper is an orthogonal material and both its strength and modulus in the MD and the XD are not the same. Its strength is likely to drop to a quite small value (5 MPa in this case) after the strain exceeds its elongation limit in the related directions. The phenolic resin is a brittle material, whose strengths in tension and compression were taken as 60 MPa and 180 MPa, respectively. The phenolic resin was modelled as an elastic-brittle material with its strength being decreased from 180 MPa to a very low value (10 MPa for compression and 5 MPa for tension in this case) after the compressive stress exceeds 180 MPa [28].

## *Constitutive model of the woven fabric lamina*

*Non-linear relationship of woven fabric lamina under in-plane shear stress.* According to the test results of the woven fabric lamina, there is a significantly non-linear stress–strain relationship under in-plane shear loading due to the micro-cracks on the interface of the fibre and resin [30]. The non-linear stress–strain relationship of the woven fabric lamina under in-plane loading can be expressed in equation (1) in according to Hahn and Tsai [31].

$$\varepsilon_{12} = \frac{\sigma_{12}}{G_{12}} + \alpha\sigma_{12}^3 \tag{1}$$

where $\alpha$ is the non-linear constant of the material in shear and it can be obtained through fitting the test results. $\varepsilon_{12}$ and $\sigma_{12}$ are the in-plane shear strain and stress, respectively. The non-linear relationship is considered through incorporating the non-linear damage factor, $d_s$, into the finite element model in accordance with equation (2) [32,33].

$$\sigma_{12}^{(i+1)} = (1 - d_s)G_{12}\varepsilon_{12}^{(i+1)} \tag{2}$$

where

$$d_s = \frac{3\alpha G_{12}\left(\sigma_{12}^i\right)^2 - \frac{2\alpha\left(\sigma_{12}^i\right)^3}{\varepsilon_{12}^i}}{1 + 3\alpha G_{12}\left(\sigma_{12}^i\right)^2}$$

and $i$ indicates the $i$-th increment in the calculation step.

Through fitting the test results, it was found that the value of $\alpha$ is 8 for the woven fabric lamina in this study [30].

*Failure criteria of the woven fabric lamina.* According to the Yen failure criteria [34], five fibre damage mechanisms and two matrix damage mechanisms are required to be considered for the woven fabric lamina. Incorporating the non-linear relationship of the woven fabric lamina under in-plane shear stress, the Yen failure criteria can be modified as follows:

1. Fill fibre damage under combined uniaxial tension and transverse shear

$$r_1^2 = \left(\frac{E_1\langle\varepsilon_1\rangle}{S_1^T}\right)^2 + \left(\frac{G_{13}\varepsilon_{13}}{S_{13}}\right)^2 = 0 \tag{3}$$

2. Warp fibre damage under combined uniaxial tension and transverse shear

$$\mathrm{r}_2^2 = \left(\frac{\mathrm{E}_2\langle\varepsilon_2\rangle}{\mathrm{S}_2^{\mathrm{T}}}\right)^2 + \left(\frac{\mathrm{G}_{23}\varepsilon_{23}}{\mathrm{S}_{23}}\right)^2 = 0 \tag{4}$$

3. Fill fibre damage under combined uniaxial compression

$$r_3^2 = \left(\frac{E_1\left\langle -\varepsilon_1 - \langle -\varepsilon_3\rangle\frac{E_3}{E_1}\right\rangle}{S_1^C}\right)^2 = 0 \tag{5}$$

4. Warp fibre damage under combined uniaxial compression

$$\mathrm{r}_4^2 = \left(\frac{\mathrm{E}_2\left\langle -\varepsilon_2 - \langle -\varepsilon_3\rangle\frac{\mathrm{E}_3}{\mathrm{E}_2}\right\rangle}{\mathrm{S}_2^{\mathrm{C}}}\right)^2 = 0 \tag{6}$$

5. Fibre damage under transverse compression

$$\mathrm{r}_5^2 = \left(\frac{\mathrm{E}_3\langle -\varepsilon_3\rangle}{\mathrm{S}_3^{\mathrm{C}}}\right)^2 = 0 \tag{7}$$

6. Matrix damage under in-plane shear stress

$$r_6^2 = \left(\frac{(1-d_s)G_{12}\varepsilon_{12}}{S_{12}}\right)^2 = 0 \tag{8}$$

7. Delamination due to through-the-thickness tensile and shear stresses

$$r_7^2 = \left(\frac{E_3\varepsilon_3}{S_3^T}\right)^2 + \left(\frac{G_{23}\langle\varepsilon_{23}\rangle}{S_{23}+S_{SR}}\right)^2 + \left(\frac{G_{13}\langle\varepsilon_{13}\rangle}{S_{13}+S_{SR}}\right)^2 \tag{9}$$

In the above equations, $\varepsilon_1$, $\varepsilon_2$ and $\varepsilon_3$ are the normal strains of the woven fabric lamina in fill, warp, and thickness directions, respectively. $\varepsilon_{12}$, $\varepsilon_{23}$, and $\varepsilon_{13}$ are the shear strains. Here, $< >$ are Macaulay brackets and conform to the equation (10).

$$< x > = \begin{cases} x, & x > 0 \\ 0, & x \leq 0 \end{cases} \tag{10}$$

$$S_{SR} = E_z \tan\varphi \langle -\varepsilon_z \rangle \tag{11}$$

where $\varphi$ is the Coulomb's friction angle.

The failure criteria of the woven fabric lamina were incorporated into Ls-Dyna by using a VUMAT subroutine.

## *Mesh generation and boundary conditions*

The finite element model of the Nomex honeycomb-cored sandwich structure with the same configuration of Specimen 1 subjected to impact loading was developed using the commercial finite element code, LS-Dyna [35], which is shown in Figure 8. The linear eight-noded brick elements with enhanced hourglass control

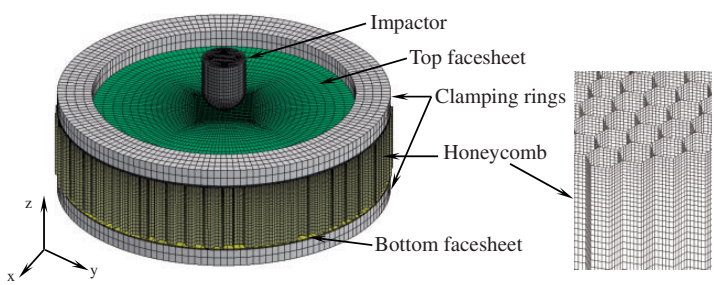


**Figure 8.** Finite element model: the global view of the model (left) and (b) the detailed view.

and reduced integration, C3D8R, were used to model the woven fabric composite facesheets to avoid the shear locking problem and to increase the computing efficiency. The modelling method of one element per ply lamina of the facesheets provides a reasonable approximation of the through-thickness stresses of the composite laminates. The walls of the Nomex honeycomb core are modelled as three-dimensional shell elements using the Part Composite tool of the LS-Dyna in accordance with the real geometric characteristics of the Nomex paper. There are three integration points through the thickness direction for the single cell wall, and five for the double cell wall. There are 34,798 elements and 36,780 nodes for the impactor, 2560 elements and 4800 nodes for the clamping rings and 28,480 elements and 41,047nodes for the two facesheets. There are also 238,784 elements and 212,856 nodes for the Nomex honeycomb core. The two rings and the impactor are modelled as analytical rigid bodies. Both rings were fixed in all 6 DOFs (*Ux*, *Uy*, *Uz*, *Rx*, *Ry*, and *Rz*) and the impactor was fixed in two translational directions (*Ux* and *Uy*) and all three rotational directions (*Rx, Ry,* and *Rz*), while an initial velocity was applied downward in *Uz* direction to obtain the impact energy.

## Contact relationships

Tie constraints were used to define the bonding conditions between the core and the two facesheets. Eroding contact was employed to model the interaction between the impactor and the facesheets. Coulomb's Friction law was used to describe the friction between the impactor and the facesheets, with the friction coefficient set to be 0.1 in accordance with Herrington and Sabbaghian 36].

The same contact relationship was also used to define the interface between the impactor and the core. The surface-to-surface contact was utilized to describe the contact relationships between the facesheets and the clamping rings. Moreover, self-contact was used to define the possible contact between the cell walls of the core during the crushing with a friction coefficient of 0.1 [37].

## Validation

The measured and simulated impact force–displacement and impact force–time curves of the cases with different impact energies are shown in Figure 9. Clearly, the simulated results agree well with the experimental results through the entire impact stage.

Table 4 shows the comparison of damage and deformation patterns of the top facesheet obtained from the simulations and tests, with reasonably good correlation. When the impact energy is 2.9 J, the damage pattern of the facesheet is a large indentation but without perforation. When it is increased to 4.9 J, the facesheet is fully perforated with cross cracks. With the further increase of impact energy to 9.9 J, the damage is expanded to a larger area. The size of the damaged area on the top facesheet related to the impact energies of 4.9 and 9.9 J is almost the

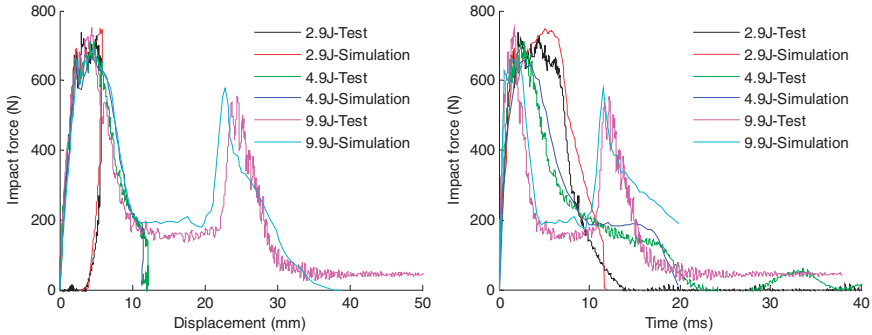


**Figure 9.** Comparisons of impact response subjected to different initial impact energies: impact force–displacement curves (left) and impact force–time curves (right).

same. This indicates that the damaged area on the top facesheet increases with the impact energy prior to the onset of the full perforation, as expected. However, when the energy is high enough to perforate the facesheet, the damaged area remains constant underneath the impactor during the perforation. The honeycomb core is crushed to a folded pattern and is torn by the shear stress around the impactor boundary, as the Nomex paper is very brittle.

Table 5 shows the experimental and simulated cross-sectional damage patterns of the honeycomb sandwich structures subjected to various impact energies. It is clearly shown that good correlation is obtained when the impact energy is 2.9 J. There are some difference between the test and simulation results of the 4.9 J and 9.9 J impacts. The possible reason is that the sandwich structures likely have some sprang back after the impactor was pulled out, which shows some recovery of the specimen. In general, based on the results shown in Tables 4 and 5, the simulations agree well with the experimental results, in terms of the deformation mode and failure mode through the entire impact.

## The effect of impact angles

Using the validated finite element models, the response of the honeycomb subjected to oblique impact is investigated, since such impact is difficult to conduct in the experiment. Figure 10 shows the definition of the angles of oblique impact, in which the 'o' is the centre point of the top facesheet, which is also the initial impacting contact point. The coordinate with x, y, and z axes is the reference system for the sandwich structure, while that with 1, 2, and 3 axes is the one for the lamina made of the facesheets and that with L, W, and T axes is for the Nomex honeycomb. 'θ' is the angle of obliquity, which is defined as the angle subtended by the velocity vector of the impactor and the normal to the surface of the sandwich structure. 'ψ' is the angle between the impact plane and the 'L' direction of the Nomex honeycomb. '$\varphi$' is the angle between the impact plane and the '1' direction of lamina with $0^\circ$ ply angle.

**Table 4.** Comparisons of the damage and deformation pattern of the top facesheet.

| Impact energy | Test results | Simulation results |
|---|---|---|
| 2.9 J |  | 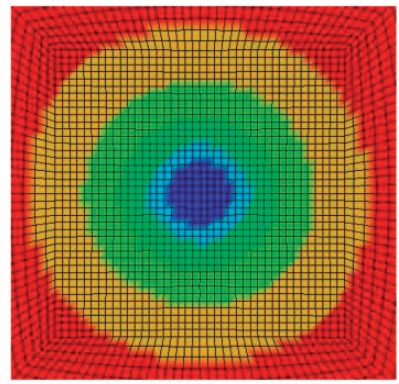 |
| 4.9 J |  | 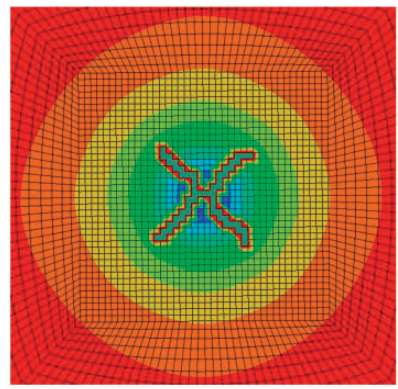 |
| 9.9 J | 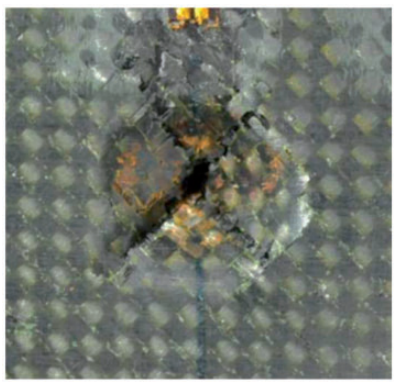 | 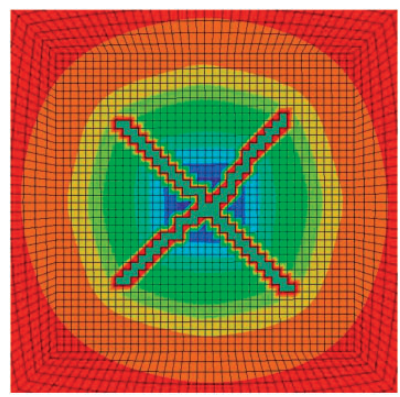 |

**Table 5.** Comparisons of the deformation results of the honeycomb sandwich.

| Impact energy | Test results | Simulation results |
|---|---|---|
| 2.9 J |  |  |
| 4.9 J |  |  |
| 9.9 J | 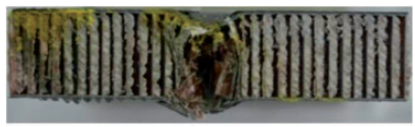 |  |

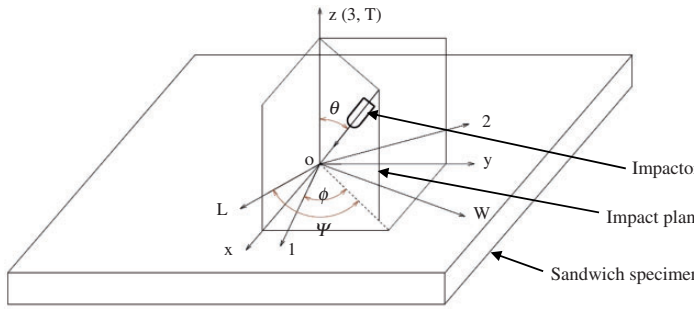


**Figure 10.** Diagram of oblique impact.

## *The effect of the angle θ*

The simulated results of five impact simulations with the varied angle θ but the same other parameters, i.e. impact energy = 9.9 J, $\varphi = 45^\circ$ and $\psi = 0^\circ$, are shown in Figure 11. Clearly, both the impact depth and the impact resistance decrease greatly with the increase of the impact angle θ. This is attributed to the reduction of resistance offered by the honeycomb core when it is struck with an angle increasingly away from its 'T' axis.

The deformation and failure modes of the oblique impact cases are shown in Figure 12. From the figure, it can be seen that both the top and bottom facesheets

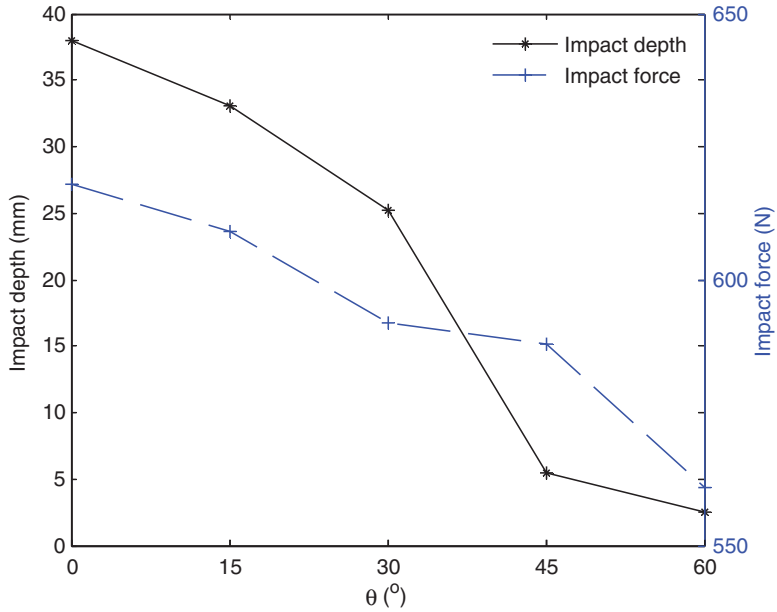


**Figure 11.** Impact depth and impact force versus the oblique impact angle. (a) 0° (b) 15° (c) 30° (d) 45° (e) 60°.

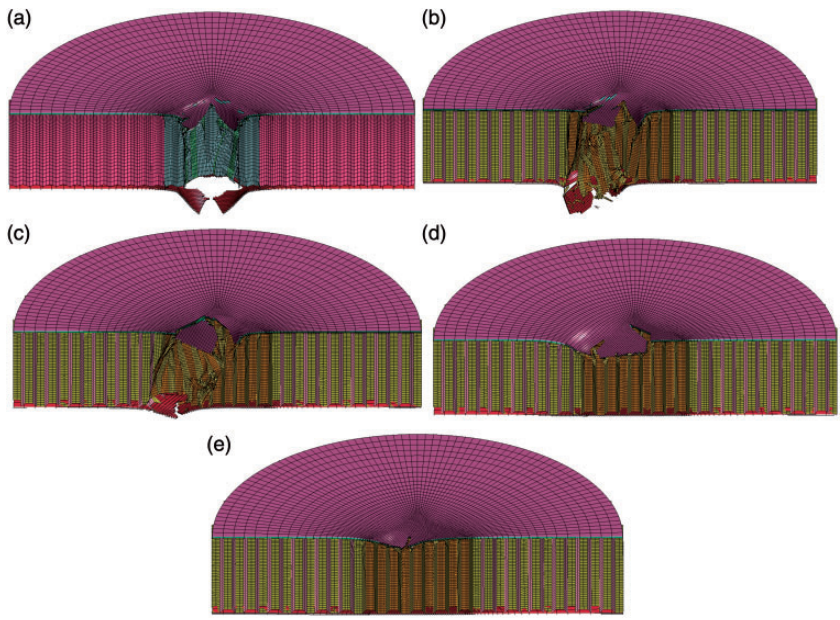


**Figure 12.** Failure and deformation at different obliquities.

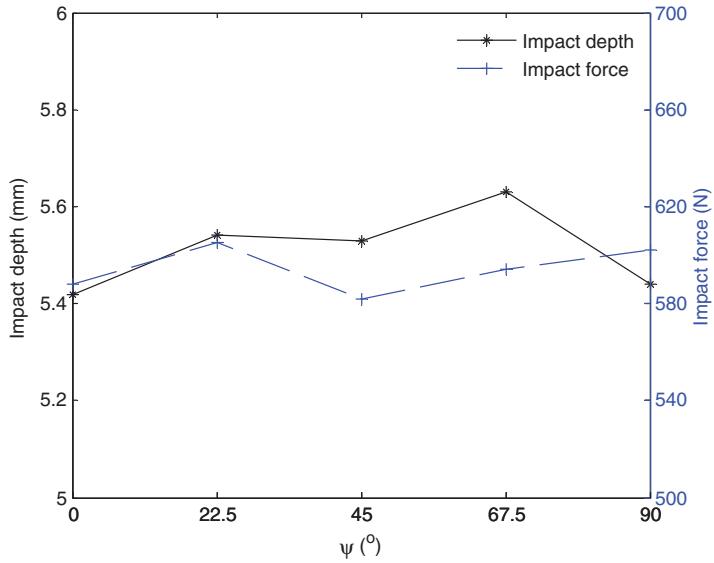


**Figure 13.** Impact results of different $\psi$.

are fully perforated when the angles of obliquity are 0° and 15°. When the angle is increased to 30°, the bottom facesheet is not fully perforated, followed by the impactor rebounding back. However, when the oblique impact angle is further increased to 45° and beyond, the top facesheet is partially damaged but not perforated. This is understandable since the velocity component in normal direction of the facesheet is getting lower with the increase of the oblique angle.

## *Effect of the angle $\psi$*

Five impact simulations with different angle $\psi$ but the same other parameters (impact energy is 9.9 J, $\theta = 45°$ and $\varphi = 0°$) were conducted and the results are shown in Figure 13. Observation of the figure points out that both the impact depth and force in the out-of-plane direction of the sandwich change little with the different impact angle $\psi$. This indicates that the angle between the orientation of the Nomex honeycomb core and the impacting direction has little influence on the impacting process and results.

## *Effect of the angle $\varphi$*

Figure 14 shows the simulation results in relation to varying the angle $\varphi$, but keeping the impact energy as 9.9 J, $\theta$ as 45°, and $\psi$ as 0°. It can be clearly seen that the impact depth decreases with the angle $\varphi$; however, the impact force in the out-of-plane direction of the sandwich increases with it. The maximum and minimum impact depths are 9.22 mm and 5.42 mm, respectively, in this range of the

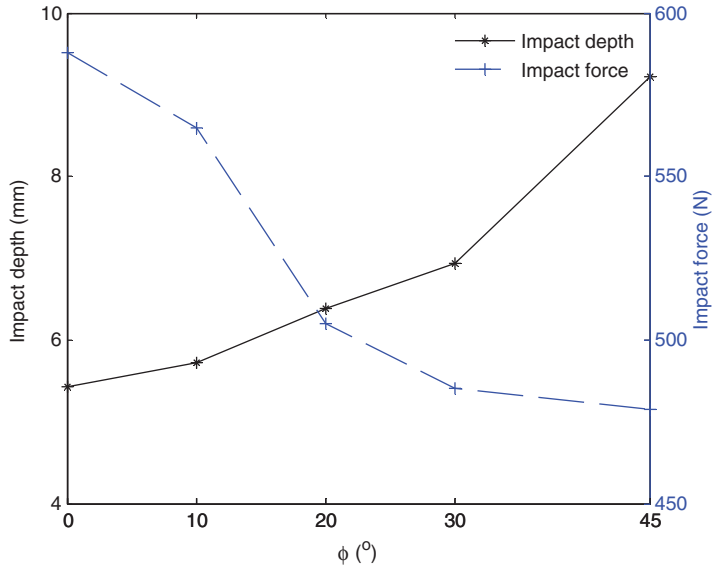


**Figure 14.** Impact results of different $\varphi$.

angle $\varphi$, while the corresponding impact forces are 588.2 N and 478.6 N, respectively. The effects of the angle $\varphi$ on both the impact depth and force are great. This is reasonable since the ply angles of the composite facesheets are all 45° and the impact plane is coincident with the fill direction of the woven fabric laminas as the impact angle $\varphi$ is 45°. This indicates that the angle between the impact direction and the fibre direction of the facesheets has a significant influence on the impact response.

## Conclusions

Based on the above study, conclusions may be drawn as follows:

1. Both the impact resistance and the perforation depth are significantly influenced by the impact energy, but the ultimate impact force and the contact stiffness are almost the same. With the same impact energy, the impactor mass has little influence on the impact resistance and perforation depth. The perforation force is primarily dependent on the thickness of the impacted facesheet and is generally linear with the variation of the thickness of the facesheet.
2. The impact process and results of the honeycomb sandwich are quite different in the laminates with the same thickness of the sum of the two facesheets. This indicates that the stiffness of the sandwich structure is far more influenced by the local indentation of the object impacted than the global bending deformation.

3. The perforation force of the honeycomb sandwich is less than half of the laminates with the same thickness of the sum of the two facesheets. However, the contact stiffness of the laminates is much higher than half of the honeycomb sandwich.
4. The oblique angle between the impactor and the sandwich structure influences both the impact resistance and the perforation depth greatly. The orientation of the Nomex core has little effect on the impact process and results. However, the angle between the impact direction and the fibre direction of the facesheet has a large influence on the impact response.
5. The meso-mechanical finite element model proposed in this paper can be used to analyse the effects of the geometry and material parameters of the Nomex honeycomb core, the facesheets and the impact parameters, such as the impact energy, angle, velocity, etc., on the mechanical responses.

## Declaration of conflicting interests

The author(s) declared no potential conflicts of interest with respect to the research, authorship, and/or publication of this article.

## Funding

The author(s) disclosed receipt of the following financial support for the research, authorship, and/or publication of this article: The research described in this paper was financially supported by the Shanghai Municipal Natural Science Foundation (14ZR1422500) and HT Support Foundation (14GFZ-JJ02-043).

## References

1. Kim CG and Jun E. Impact resistance of composite laminated sandwich plates. *J Compos Mater* 1992; 26: 2247–2261.
2. Zhou G, Hill M, Loughlan J, et al. Damage characteristics of composite honeycomb sandwich panels in bending under quasi-static loading. *J Sandw Struct Mater* 2006; 8: 55–90.
3. Abrate S. Localized impact on sandwich structures with laminated facings. *Appl Mech Rev* 1997; 50: 69–82.
4. Lacy TE and Hwang Y. Numerical modeling of impact-damaged sandwich composites subjected to compression-after-impact loading. *Compos Struct* 2003; 61: 115–128.
5. Aktay L, Johnson AF and Kroplin BH. Numerical modelling of honeycomb core crush behaviour. *Eng Fract Mech* 2008; 75: 2616–2630.
6. McQuigg TD. Compression after impact experiments and analysis on honeycomb core sandwich panels with thin facesheets. NASA/CR-2011-217157, 2011.
7. Zinno A, Prota A, Maio ED, et al. Experimental characterization of phenolic-impregnated honeycomb sandwich structures for transportation vehicles. *Compos Struct* 2011; 93: 2910–2924.
8. Meo M, Morris AJ, Vignjevic R, et al. Numerical simulation of low-velocity impact on an aircraft sandwich panel. *Compos Struct* 2003; 62: 353–360.
9. Manes A, Gilioli A, Sbarufatti C, et al. Experimental and numerical investigations of low velocity impact on sandwich panels. *Compos Struct* 2003; 99: 8–18.

10. Gilioli A, Sbarufatti C, Manes A, et al. Compression after impact test (CAI) on NOMEX$^{TM}$ honeycomb sandwich panels with thin aluminum skins. *Compos Part B-Eng* 2014; 67: 313–325.
11. Meng L, Chen S, Wu Y, et al. Projectile impact behaviour of sandwich material with Nomex honeycomb and metallic skins. *Adv Mater Res* 2011; 204–210: 632–635.
12. Aminanda Y, Castanie B, Barrau JJ, et al. Experimental and numerical study of compression after impact of sandwich structures with metallic skins. *Compos Sci Technol* 2009; 69: 50–59.
13. Castanié B, Bouvet C, Aminanda Y, et al. Modelling of low-energy low-velocity impact on Nomex honeycomb sandwich structures with metallic skins. *Int J Impact Eng* 2008; 35: 620–634.
14. Aktay L, Johnson AF and Holzapfel M. Prediction of impact damage on sandwich composite panels. *Comput Mater Sci* 2005; 32: 252–260.
15. Aktay L, Johnson AF and Kroplin BH. Numerical modelling of honeycomb crush behaviour. *Eng Fract Mech* 2008; 75: 2616–2630.
16. Hu J, Ma D, Le G, et al. A rate-dependent constitutive model for honeycomb material and its application in a lunar lander. *J Vibr Shock* 2014; 33: 114–119.
17. Foo CC, Chai GB and Seah LK. A model to predict low-velocity impact response and damage in sandwich composites. *Compos Sci Technol* 2008; 68: 1348–1356.
18. Menna C, Zinno A, Asprone D, et al. Numerical assessment of the impact behaviour of honeycomb sandwich structures. *Compos Struct* 2013; 106: 326–339.
19. Petras A and Sutcliffe MPF. Indentation failure analysis of sandwich beams. *Compos Struct* 2000; 50: 311–318.
20. Mohr D and Doyoyo M. Analysis of the Arcan apparatus in the clamped configuration. *J Compos Mater* 2002; 36: 2583–2594.
21. Mohr D and Doyoyo M. A new method for the biaxial testing of cellular. *Solids Exp Mech* 2003; 43: 174–183.
22. Doyoyo M and Mohr D. Microstructural response of aluminum honeycomb to combined out-of-plane loading. *Mech Mater* 2003; 35: 865–876.
23. Mohr D and Doyoyo M. Experimental investigation on the plasticity of hexagonal aluminum honeycomb under multiaxial loading. *J Appl Mech* 2004; 71: 375–385.
24. Hong ST, Pan J, Tyan T, et al. Quasi-static crush behaviour of aluminum honeycomb specimens under non-proportional compression dominant combined loads. *Int J Plast* 2006; 22: 1062–1088.
25. Hong ST, Pan J, Tyan T, et al. Dynamic crush behaviours of aluminum honeycombs specimens under compression dominant inclined loads. *Int J Plast* 2008; 24: 89–117.
26. Hexcel Composites. *HexWeb honeycomb attributes and properties*. Stamford, CT: Hexcel Corporation, 1999.
27. Heimbs S. Virtual testing of sandwich core structures using dynamic finite element simulations. *Comp Mater Sci* 2009; 45: 205–216.
28. Liu L, Wang H and Guan Z. Experimental and numerical study on the mechanical response of Nomex honeycomb core under transverse loading. *Compos Struct* 2015; 121: 304–314.
29. ASTM Committee. ASTM D 3763-02. *Standard test method for high speed puncture properties of plastics using load and displacement sensors*. West Conshohocken, PA: Author, 2002.

30. Deng Yan. *A multi-scale correlating model for predicting the mechanical properties of textile composites*. Master Thesis, Shanghai Jiao Tong University, Shanghai, 2014.
31. Hahn HT and Tsai SW. Nonlinear elastic behaviour of unidirectional composite laminate. *J Compos Mater* 1973; 7: 102–118.
32. Shokrieh MM and Lessard LB. Effects of material nonlinearity on the three-dimensional stress state of pin-loaded composite laminates. *J Compos Mater* 1996; 30: 839–861.
33. Liu W, Zhou G, Gao J, et al. Continuum damage model and damage parameter identifications for composites considering the effect of shear nonlinearity. *Acta Mater Compos Sin* 2013; 30: 221–226.
34. Yen CF. A ballistic material model for continuous-fibre reinforced composites. *Int J Impact Eng* 2012; 46: 11–22.
35. Hallquist JO. *LS-DYNA keyword user's manual, version 970*. California: Livermore Software Technology Corporation, 2007.
36. Herrington PD and Sabbaghian M. Factors affecting the friction coefficients between metallic washers and composite surfaces. *Composites* 1991; 22: 418–424.
37. Ren G, Zhang Z, Zhu X, et al. Influence of functional graphene as filler on the tribological behaviours of Nomex fabric/phenolic composite. *Compos Part A Appl Sci Manuf* 2013; 49: 157–164.